Journal of Spacecraft and Rockets
Vol. 58, No. 3, May–June 2021

Lyapunov Optimal Touchless Electrostatic Detumbling of Space Debris in GEO Using a Surface Multisphere Model

Fausto Casale*
Polytechnic University of Milan, MI 20156 Milan, Italy
Hanspeter Schaub†
University of Colorado, Boulder, Colorado 80309
and
James Douglas Biggs‡
Polytechnic University of Milan, MI 20156 Milan, Italy

https://doi.org/10.2514/1.A34787

High tumbling rates of uncooperative target pose strong technical challenges and collision risks that can prevent removal of the debris using contact, such as with robotic arms or capture nets. Electrostatic touchless detumbling is a promising technology that can be used to decrease the rotational velocity of an uncooperative object in geosynchronous orbit, from a safe distance. This paper demonstrates the advantages of applying a Lyapunov optimal control in conjunction with a surface multisphere model. This approach allows for the analysis of general shapes, eliminating the need for analytical approximations on debris shape and expected torque, employed by previous work. Moreover, using this model, the robustness of the system to uncertainties to the debris center of mass position is tested. This analysis uncovers an unstable phenomenon that was previously not captured using simpler models. An active disturbance rejection control ensures robustness of the system in the cases analyzed, also granting an increase in its effectiveness. It is shown in simulation that the system can exploit deviations in the center of mass to achieve a higher level of controllability and completely detumble all components of angular velocity.

I. Introduction

THE accumulation of space debris in Earth orbit presents a significant risk to infrastructure and human presence in space [1,2]. Active debris removal is one approach that has been proposed to mitigate this risk to existing space assets. This is especially challenging for debris in Geocentric orbit (GEO), where the perturbations due to atmospheric drag and Earth oblateness are too small to ensure natural deorbiting, compared, for example, with low Earth orbits (LEOs), where the lifetime of a debris can be significantly shorter.

The total number of inactive objects in the geostationary belt has increased considerably over the last decade, leading to an accumulation of over a thousand of debris, several meters in size, far surpassing the number of total active spacecraft in orbit (around 500) [3–5]. The value of space assets, essential for communication, in the region of GEO is estimated to be U.S. $13 billion [6], and so protecting these objects from potentially catastrophic impacts is a priority. Most concepts for deorbiting an uncooperative object involve the use of a chaser spacecraft that brings itself close to the debris, and detumbles and de-orbits it using, for example, a robotic arm or a net [7–11].

This requires the spacecraft to touch the debris, posing significant risks because the debris can be tumbling uncontrollably with rates up to 10 deg/s [12–14]. In fact, the current requirement of de-orbiting technology is estimated to be around 1 deg/s [8–11]. It is then necessary to reduce these rotations before employing the de-orbit technology. Moreover, it is desirable to do this at a safe distance from the debris itself without the requirement of contact. For this reason, different touchless detumbling strategies have been developed, like the ion-beam shepherd [15,16] or electrostatic detumbling [17–19]. Both of these methods trade the speed and effectiveness of a contact strategy for the reduced risk of impacts and ability to handle high tumbling rates. Electrostatic detumbling is examined in this paper. Electrostatic charging is used to generate forces and torques on the debris instead of using the momentum carried by the ion beam itself, as in the case of the ion-beam shepherd. This is achieved by using a service spacecraft that imposes the potential on the debris, as showed in Fig. 1.

In recent years, studies have been conducted on the feasibility of imposing an electric potential on a debris and a service spacecraft, using electron beams and ion emitters [20], and then using the electrostatic forces generated to decrease the kinetic energy of the debris touchlessly [21,22]. Schaub and Sternovsky [20] showed that this is feasible to accomplish using current technology; moreover, it is possible to charge objects to tens of kilovolts in a matter of microseconds and using as little as watts level electric power. In GEO, the charged objects are able to exert significant electrostatic forces even with separation distances of tens of meters, because Debye lengths are approximately around 200 m [23,24]. This is not possible in high-density plasma environments, such as in LEO, where the effects of Debye shielding are much more intense [25].

To predict the generated torques, and thus compute the voltage required, a multisphere model (MSM) has been developed [26]. It models the charge distribution as a population of spheres placed in various parts of the body. Based on the radius of the spheres and their position, the MSM computes the charge contained in each sphere by solving a linear system. The total forces and torques are then obtained by applying Coulomb's law between each pair of spheres created, allowing the generated torques to be predicted faster than real time. The model assumes the bodies to consist of uniform conductors, which is reasonable for most spacecraft due to the high conductivity of the external Mylar protective layers [27].

The volume MSM (VMSM) generates a small number of spheres positioned in the spacecraft volume; the radius and exact position were initially handpicked to match the electrostatic forces and fields of a high-precision finite element method (FEM) model [12]. This procedure is computationally expensive, and so automated methods have been developed to speed up the procedure [28,29], but it still requires a complex truth model to match. Moreover, this method is

---

Received 20 February 2020; revision received 3 October 2020; accepted for publication 19 January 2021; published online 5 May 2021.

*Postgraduate Student, Department of Aerospace Science and Technology; fausto.casale@polimi.it.

†Professor and Glenn L. Murphy Chair of Engineering, Department of Aerospace Engineering, ECNT 321, 431 UCB.

‡Associate Professor, Department of Aerospace Science and Technology.

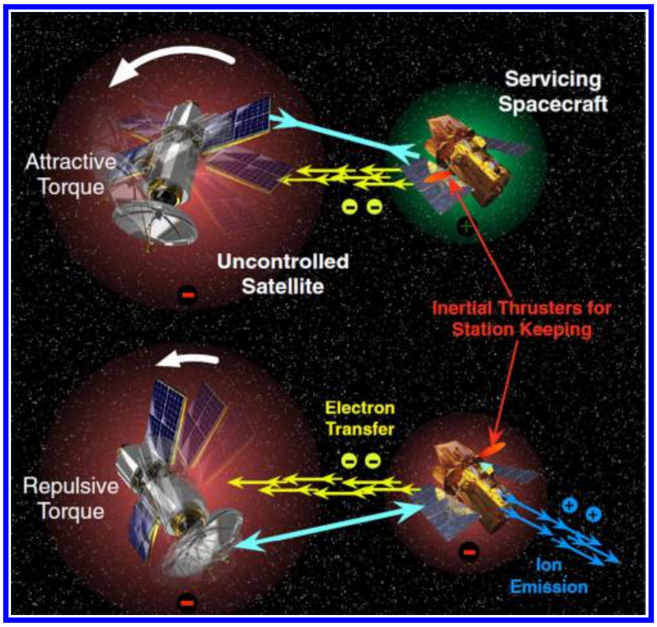

Fig. 1 Service spacecraft imposing an electric potential to the debris. (Figure taken from [12].)

better suited for simple shapes, like the one depicted in Fig. 2, where no torque around the symmetry axis was considered. This led to previous control laws to assume a certain expected analytical torque function that depends on the inclination of the cylinder axis, completely ignoring any possible effect on the angular velocities around the symmetry axis [17–19]. It is also possible to generate more precise models by increasing the number of spheres distributed in the volume of the object, thus granting a better description of the torque in all axes, but again the position in which the spheres are generated can be arbitrary and complex to implement. Using an analytical function to describe the obtained torque is useful to find equilibrium points and analyze the general behavior of the system, but it can limit the flexibility of the analysis.

For this reason, the next advancement switches to generating a greater number of spheres on the conductor surface, and is thus called surface MSM (SMSM) [30]; it is faster to set up and it yields more precise torque estimations with just a small increase of computational effort. Also, it represents more accurately the behavior of real electric charges that always position themselves on the surface of the objects.

This paper implements the method developed in [31] to generate SMSM of complex shapes and simulate detumbling by computing the generated forces and torques by directly applying Coulomb's law on each sphere, instead of relying on a torque analytical function. The control strategy employed is a Lyapunov optimal controller that aims to obtain the fastest decrease of kinetic energy possible, by selecting the correct voltage to impose at each time step. This new control law is also able to handle general spacecraft tug and debris geometries, because it does not rely on any shape assumption. The robustness of the system to uncertainties is analyzed and the application of an active disturbance rejection control (ADRC) [32–35], which estimates the lumped uncertainties accounting for them in the control, is tested.

II. Multisphere Model Generation Procedure

An SMSM is generated for the two objects considered: the service spacecraft and the debris. First, a triangular surface mesh is created, and then the method of moments (MOM) is applied to the mesh to generate the sphere distribution. The MOM is an analytical model employed to compute the charge on the mesh elements described in [31].

A. Mesh Generation

A triangular mesh that describes the object external surface as a series of triangles is generated; the higher the number of triangles used, the more precise the model, with a higher number of spheres generated, and thus a higher computational complexity to the simulation. These meshes can be created manually, generating each vertex and edge, but this is only feasible when using very simple shapes, like cubes and cylinders. It is far easier to use a 3-D modeling software to create .stl files manually or starting from already existing 3-D CAD models.

The software used during this study is 3D Builder [36], usually used for 3-D printing, and so each part of the system can be customized to have as many triangles as necessary. By changing only a few parameters, it is possible to create .stl files of many different numbers of total triangles for the same shape, even with a heterogeneous distribution, for example, by concentrating most spheres on the parts closer to the debris (Fig. 3c). The meshes are also modified using MeshLab [37] to refine some aspects and delete triangles that may not be necessary.

B. From MOM to SMSM for the Isolated Object

Once the mesh is created, the MOM is used to compute the charge distribution on each of the N triangles the surface is divided into, by solving the Gauss theorem on each triangle (for a more in-depth description, see [31]):

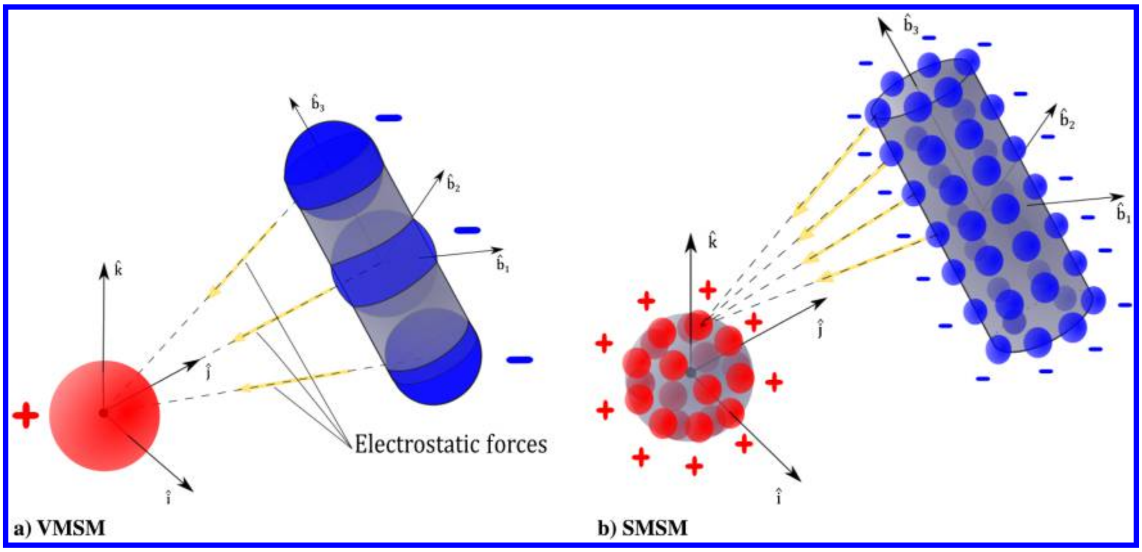

a) VMSM

b) SMSM

Fig. 2 Same geometry represented using the two MSMs.

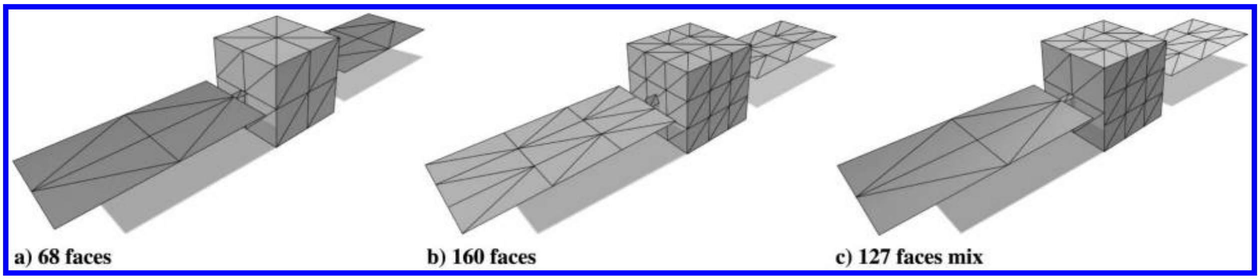
a) 68 faces b) 160 faces c) 127 faces mix

Fig. 3 Three different levels of mesh precision.

$$V(r) = \int \frac{\mathrm{d}q'}{4\pi\epsilon_0 \|\boldsymbol{r} - \boldsymbol{r}'\|} \tag{1}$$

Then, for all the triangles, the following linear system is built:

$$\begin{bmatrix} V_1 \\ V_2 \\ \vdots \\ V_N \end{bmatrix} = \frac{1}{4\pi\epsilon_0} \begin{bmatrix} \int_{A_1} \frac{\mathrm{d}A}{\|\boldsymbol{r}_1 - \boldsymbol{r}'\|} & \int_{A_2} \frac{\mathrm{d}A}{\|\boldsymbol{r}_1 - \boldsymbol{r}'\|} & \cdots & \int_{A_N} \frac{\mathrm{d}A}{\|\boldsymbol{r}_1 - \boldsymbol{r}'\|} \\ \int_{A_1} \frac{\mathrm{d}A}{\|\boldsymbol{r}_2 - \boldsymbol{r}'\|} & \int_{A_2} \frac{\mathrm{d}A}{\|\boldsymbol{r}_2 - \boldsymbol{r}'\|} & \cdots & \int_{A_N} \frac{\mathrm{d}A}{\|\boldsymbol{r}_2 - \boldsymbol{r}'\|} \\ \vdots & \vdots & \ddots & \vdots \\ \int_{A_1} \frac{\mathrm{d}A}{\|\boldsymbol{r}_N - \boldsymbol{r}'\|} & \int_{A_2} \frac{\mathrm{d}A}{|\boldsymbol{r}_N - \boldsymbol{r}'|} & \cdots & \int_{A_N} \frac{\mathrm{d}A}{\|\boldsymbol{r}_N - \boldsymbol{r}'\|} \end{bmatrix} \begin{bmatrix} Q_1 \\ Q_2 \\ \vdots \\ Q_N \end{bmatrix}$$

$$\boldsymbol{V} = [S]\boldsymbol{Q} \quad \boldsymbol{Q} = [C]\boldsymbol{V} \tag{2}$$

Thanks to the square matrix in the preceding system (called elastance matrix $[S]$), it is possible to relate the potential on each element of the object to the charge accumulated on it. In this study, the potential is assumed equal for all elements $V_1 = V_2 = V_N = V_{\mathrm{body}}$, then to compute the resulting charge, the elastance $[S]$ is inverted to obtain the capacitance matrix $[C]$.

This procedure, although giving accurate results, is computationally heavy because it requires one to solve $N \times N$ integrals at each sampling time. Therefore, this is only done once to set up the parameters for the SMSM by matching the elements of $[S]$.

This is possible because the SMSM relates potential and charge in the system in a similar way, with the following linear system:

$$\begin{bmatrix} V_1 \\ V_2 \\ \vdots \\ V_N \end{bmatrix} = \frac{1}{4\pi\epsilon_0} \begin{bmatrix} 1/R_1 & 1/r_{1,2} & \cdots & 1/r_{1,N} \\ 1/r_{2,1} & 1/R_2 & \cdots & 1/r_{2,N} \\ \vdots & \vdots & \ddots & \vdots \\ 1/r_{N,1} & 1/r_{N,2} & \cdots & 1/R_N \end{bmatrix} \begin{bmatrix} Q_1 \\ Q_2 \\ \vdots \\ Q_N \end{bmatrix} \tag{3}$$

As it can be seen, the charge on each i sphere depends only on its radius R_i and the distance from all the other spheres $r_{i,j}$, and so the matrix $[S]$ stays constant as long as the object does not change its shape. The radius of the sphere is obtained by inverting the diagonal elements of the $[S]$ matrix given by the MOM; the spheres are then positioned at the centroid of each triangle, and this leads to good matching of all the elements of the two $[S]$ matrices, if the mesh has an appropriate amount of triangles; otherwise, the errors increase noticeably.

The resulting matrix is mostly diagonal unless the radius of the spheres is too big compared to the sphere distance (Spheres should not intersect.), leading to singularity effects when computing the inverse. The elements of this matrix only depend on the geometric properties of the isolated body and are conserved during rigid-body rotations or translations, and so they can be computed only once during the preprocessing phase, as demonstrated in [27,38]. Because of this property, the $[S]$ matrix referred to the single body is called the self-elastance matrix.

C. Capacitance Matching and Two-Body Setup

The total capacitance of the isolated body is computed by summing all the elements of the self-capacitance matrix $[C]$; this increases the performance of the simulation, as stated in [31]. Scaling the computed radius of the spheres to obtain the same total capacitance of a truth model (FEM model or high-number SMSM) increases the precision of the computed torques and forces without increasing the computational effort.

So, the radii of the SMSM obtained are scaled up, by a radius parameter α, until the total capacitance matches the desired value or at least comes as close as possible without leading to any numerical instabilities (depicted in Fig. 4); once this has been done for both bodies considered (service craft and debris), the two can be put together to compute the interactions between the charged elements.

In particular, the charge will redistribute based on the distance between each sphere that is changing with the debris tumbling motion. The obtained linear system can be summed up to obtain

$$\begin{bmatrix} \boldsymbol{V}_1 \\ \boldsymbol{V}_2 \end{bmatrix} = \begin{bmatrix} [S_1] & [Sm] \\ [Sm]^T & [S_2] \end{bmatrix} \begin{bmatrix} \boldsymbol{Q}_1 \\ \boldsymbol{Q}_2 \end{bmatrix} \tag{4}$$

where $[S_1]$ $(N \times N)$ and $[S_2]$ $(M \times M)$ are the constant self-elastance square matrices of the service and debris, respectively, and the elements of $[Sm]$ are made up by the inverse of the distance between the spheres of the two different bodies, and these are the elements that change during the tumbling motion. Also, $\boldsymbol{V}_1$ and $\boldsymbol{V}_2$ represent vectors with the imposed potential for each sphere of the two bodies, same for charge vectors $\boldsymbol{Q}_1$ and $\boldsymbol{Q}_2$.

Given this particular structure of the total elastance matrix, the Schur complement method can be used to obtain the capacitance matrix without having to recompute the full matrix at each time step:

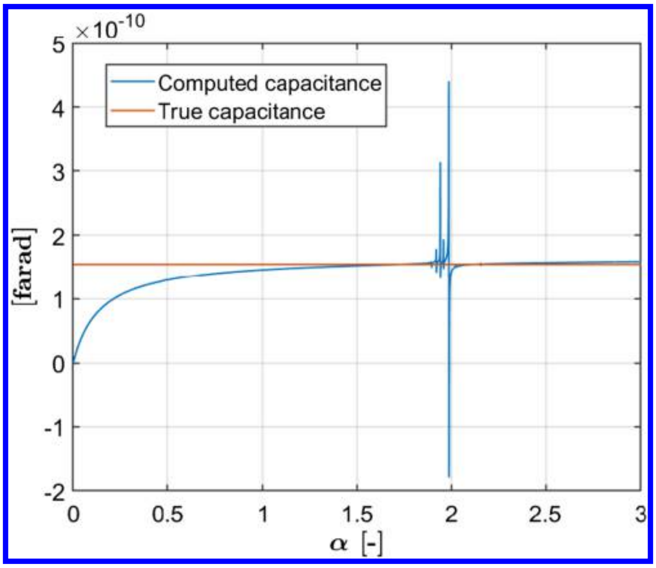

Fig. 4 How capacitance changes by scaling the radii of the SMSM of a parameter α.

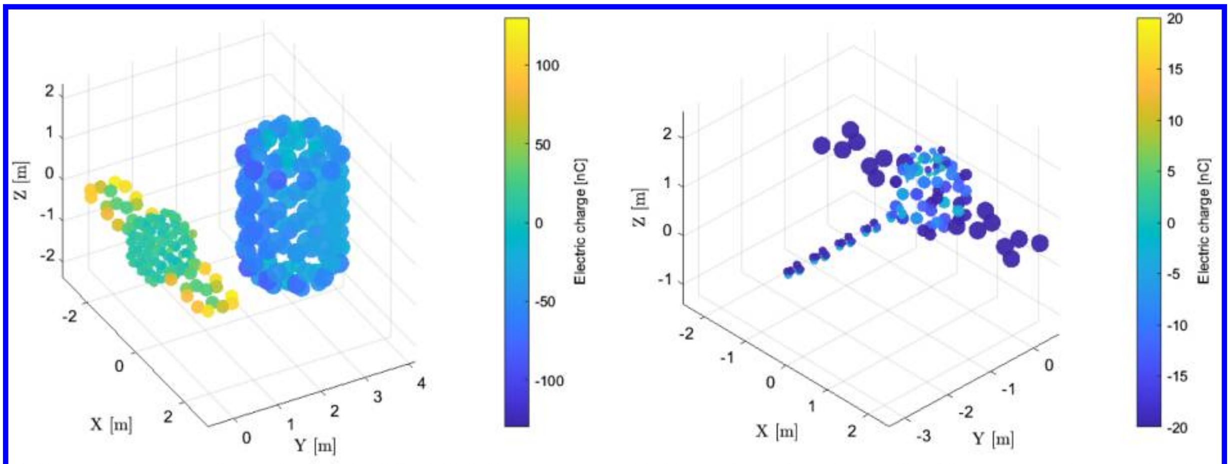

a) Box and panel servicecraft and cylindrical debris

b) Box and panel servicecraft with antenna and magnetometer boom

Fig. 5 Examples of SMSM.

$$\begin{pmatrix} A & B \\ C & D \end{pmatrix}^{-1} = \begin{pmatrix} (A - BD^{-1}C)^{-1} & -(A - BD^{-1}C)^{-1}BD^{-1} \\ -D^{-1}C(A - BD^{-1}C)^{-1} & (D - CA^{-1}B)^{-1}) \end{pmatrix} \tag{5}$$

Once the charge distribution is obtained, the forces and resulting torques for each sphere pair (N spheres on service craft and M spheres on debris) are computed using Coulomb's law, and the total torques acting on the bodies are obtained:

$$\boldsymbol{F}_j = \sum_{i=1}^{N} \frac{1}{4\pi\epsilon_0} \frac{Q_i Q_j}{r_{ij}^3} \boldsymbol{r}_{ij} \tag{6}$$

$$\boldsymbol{L} = \sum_{j=1}^{M} \boldsymbol{r}_{j|b} \times \boldsymbol{F}_j \tag{7}$$

First, the total force $\boldsymbol{F}_j$ on each j sphere of the debris is computed by summing all Coulomb contributions from each i sphere of the service. Then, the total torque $\boldsymbol{L}$ acting on the debris is obtained by summing up all the contributions given by the cross product between the position of the j sphere in body coordinates $\boldsymbol{r}_{j|b}$ and the total force resulting on it $\boldsymbol{F}_j$.

With this, the setup of the SMSM is completed (Fig. 5). In the next section, a description of the dynamic system is provided, and then the chosen parameters and first results are given.

III. System Dynamics and Control Strategy

The system uses two different frames of reference, depicted in Fig. 2: a fixed one called $\mathcal{N}$ ($\boldsymbol{i}$, $\boldsymbol{j}$, $\boldsymbol{k}$) that is centered in the service spacecraft center of mass (c.m.), and a body frame $\mathcal{B}$ ($\boldsymbol{b}_1$, $\boldsymbol{b}_2$, $\boldsymbol{b}_3$) centered at the debris c.m. that is initially set at a certain distance d on the axis $\boldsymbol{j}$. Only rotations of the debris are considered; this is because the service spacecraft is assumed to use thrusters to offset the resulting torques on it, and this assumption can be considered reasonable given the low intensity of the resulting torques (around 10^{-7} N · m for the symmetry axis and 10^{-4} N · m for the others). Also, the same thrusters are assumed to be able to keep the separation distance imposed, as demonstrated in [22].

A. System Description

The system architecture is depicted in Fig. 6. At each time step, the relative attitude between the two frames is described by the direction cosine matrix $A_{B/N}$ and used to compute the resulting electrostatic torques on the debris using the SMSM.

In particular, the torques are first computed by the controller, which selects the electric potential to impose on the objects based on a less precise sphere population (Fig. 3a), and then this potential is given to the physics model that computes the real value of the resulting torques, using a better sphere model (Fig. 3b), which are then applied to the system.

Thanks to the customization proprieties of the SMSM, it is thus possible to mimic the modeling errors that are present in a real case and study their effect on the system performance. Ideally, the physics population would have a very high number of sphere count to better represent the real charge distribution, but this is limited by the performances of the machine used to run the simulation.

Also, no uncertainties in angular velocity reading or attitude imprecision are included. It is assumed that the service spacecraft is able to reconstruct the debris state using cameras or LIDAR with an error well below 0.1 deg/s for velocity and 10 cm for the position of the debris, which would not contribute significantly to the performance of the detumble; this is a reasonable assumption, given the precision granted by modern imaging systems [39–41].

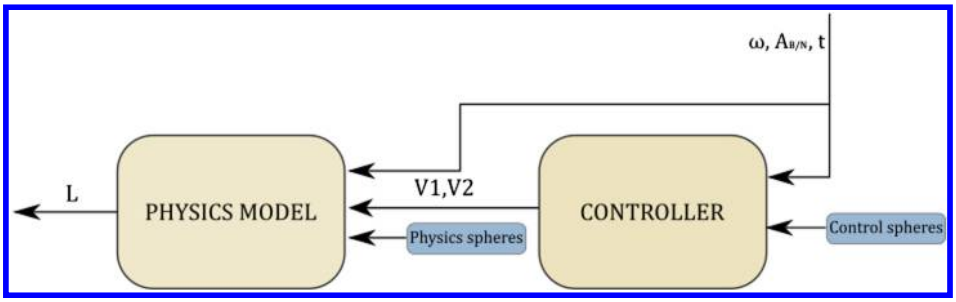

Fig. 6 Controller and physics simulation structure.

After the electrostatic torque is computed, more effects can be added, like solar radiation pressure torques, gravity gradient, and c.m. deviations; this way, it is possible to study the effects these aspects have on the debris and the detumbling performance.

B. Control Law

The Lyapunov optimal control law used to ensure the detumbling of the debris is based on the minimization of the Lyapunov function $V(\boldsymbol{\omega})$ [42], defined as the expected total kinetic energy of the debris; from now on, all estimated quantities that make up the controller model are identified with an asterisk:

$$V(\boldsymbol{\omega}) = T^* = \frac{1}{2}\boldsymbol{\omega}^T[J]\boldsymbol{\omega}$$

$$\dot{V}(\boldsymbol{\omega}) = \dot{T}^* = \boldsymbol{\omega}^T[J]\dot{\boldsymbol{\omega}} = \boldsymbol{\omega}^T([J]\boldsymbol{\omega}\times\boldsymbol{\omega} + \boldsymbol{L}^*) = \boldsymbol{\omega}^T\boldsymbol{L}^* \tag{8}$$

The angular velocity $\boldsymbol{\omega}$, the torque $\boldsymbol{L}^*$, and inertia matrix $[J]$ are expressed along the principal axes in body coordinates; also, the term $[J]\boldsymbol{\omega}\times\boldsymbol{\omega}$ is deleted because it is perpendicular to $\boldsymbol{\omega}$, and thus its scalar product goes to zero.

The expected torque $\boldsymbol{L}^*$, which is different from the real one evaluated in the physics model, depends on the imposed potential on the two objects, and so the Lyapunov derivative also depends on the chosen potential V_1 for the spacecraft and V_2 for the debris.

Initially, the controller was given the ability to pick both potentials from an interval of ±20 kV, but first results showed that $\dot{T}^*$ varies almost linearly with the imposed potential, as it can be seen in Fig. 7, and also that the value does not change if the two potentials V_1 and V_2 are swapped. Because the objective of the detumbling is to decrease the kinetic energy as fast as possible without a real interest in the final attitude of the debris, only the maximum values of ±20 kV are evaluated for the service spacecraft and the debris is kept at a constant 20 kV, effectively limiting the controller to a bang-bang control.

So, at each time step, the controller computes the resulting $\dot{T}^*$ for positive and negative imposed potentials, selecting the one that ensures a negative value of $\dot{T}^*$; if neither of the two potentials grants the desired negative derivative, the controller sets both potentials to zero to avoid any possible increase of the kinetic energy of the system.

This only works as long as the controller is able to correctly predict the torque; if the prediction is off by a big-enough value, the debris kinetic energy could actually increase, leading to instability in the system.

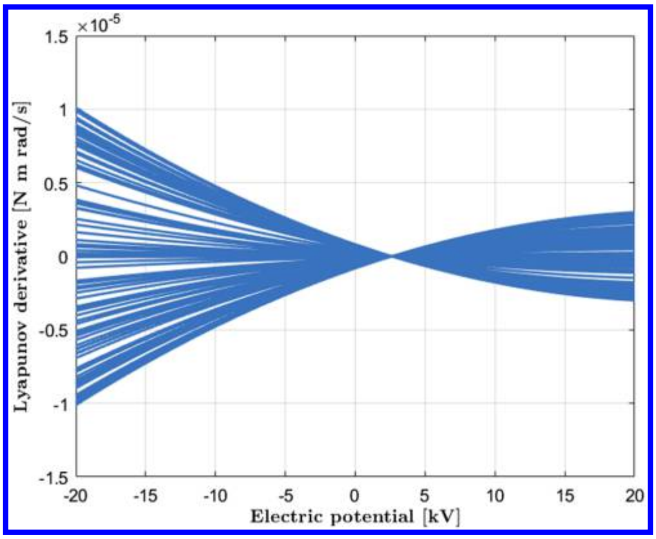

Fig. 7 Lyapunov derivative variation with imposed potential for first 100 time steps.

This can be easily understood by adding and subtracting the computed Lyapunov derivative $\dot{T}^*$ to the real kinetic energy derivative:

$$T = \frac{1}{2}\boldsymbol{\omega}^T[J]\boldsymbol{\omega}$$

$$\dot{T} = \boldsymbol{\omega}^T[J]\dot{\boldsymbol{\omega}} = \boldsymbol{\omega}^T\boldsymbol{L} = \boldsymbol{\omega}^T(\boldsymbol{L} + \boldsymbol{L}^* - \boldsymbol{L}^*) = \boldsymbol{\omega}^T\boldsymbol{L}^* + \boldsymbol{\omega}^T\boldsymbol{\epsilon}_L \tag{9}$$

The real kinetic energy derivative consists of a first term that is negative because the controller ensures so, and a second one that depends on the error in torque estimation $\boldsymbol{\epsilon}_L$; this could either be negative or positive, depending on the error and could, if bigger than the first term, bring the kinetic energy derivative up to positive values.

Nevertheless, the torque estimation is good enough if an appropriate number of spheres are set, to avoid this from happening. It can also be seen that if the expected torque is high, the margin for error is also higher, and so systems where the torques generated are higher can ensure a correct detumbling with higher error values. This means that larger objects may take longer to detumble because of the bigger inertia, but also are more stable to errors in the estimation of torques; also, this holds true for different torque components in the same object. For example, in the case of the cylindrical debris, the rotations around the symmetry axis $\boldsymbol{b}_3$ should be less stable because the torques generated are very low.

This hypothesis is later confirmed by the results obtained in Sec. IV.

C. Ideal Case Simulation

The method developed has been applied initially to the simple geometry case with a cylindrical debris of height 3 m and radius 1 m and spherical service spacecraft of radius 2 m, to compare the results with the ones obtained with the VMSM in previous papers [12]. For that reason, the same initial conditions have been used here and throughout the rest of the cases analyzed; all the parameters used are provided in the Appendix. To select the appropriate amount of spheres for the two objects, the transversal and symmetry axis torques have been computed for different sphere counts, resulting in the graphs represented in Fig. 8.

As it can be seen, the torque computed stays within 2% of the truth value for the transversal torque after more than 100 spheres are considered, but it can change considerably for the symmetry axis one.

The net torque can even change sign from one model to the other if a poorly designed mesh is chosen, as it can be seen in the Fig. 8, highlighted by the blue line. This can be avoided by carefully picking a mesh that is as symmetrical as possible, leading to a correct modeling of the torque that is also more robust to uncertainties.

In these first two cases, the same numbers of spheres have been used in the physics model: 112 for the debris and 100 for the service. Also, the objects are at 10 m distance. (Less spheres are necessary for this simpler geometry than in the box panel service case.) Because both simulations give the same exact results, there is only one set of figures.

These are consistent with the previous experience, with the kinetic energy of the debris decreasing monotonically until the only component of angular momentum remaining is the one along the $\boldsymbol{j}$ axis, thus along the line that links service and debris. Using an SMSM model for the controller, instead of a VMSM, does not seem to influence the results obtained, and so in this case, the SMSM does not provide any particular advantage beside an increased precision of the torques itself. This confirms the validity of the VMSM when dealing with simple shapes, because it gives the exact same results.

Moving to a more complex geometry, with a cubic service spacecraft provided with two solar panels (As seen in Fig. 5a). It is possible to observe how the angular velocity of the debris does not stay constant after the initial decrease, but continues to fall very slowly in time. Also, the component of angular momentum H_j is not constant anymore even if the time it would take to go completely to zero is in the order of months/year. (The simulation time in Fig. 10 is more than double the one in Fig. 9.) This demonstrates that the controller is able to use the small torques generated around $\boldsymbol{j}$ by the geometry and induced effects, effectively granting a higher level of control on the debris.

Nevertheless, this effect is not exploitable, given the long times it takes to bring the kinetic energy down, and is not really relevant in the case of a geostationary orbit, where the two bodies do not stay fixed in the inertial frame, but have a time-varying relative position in a leader–follower orbit that greatly improves the capability of the system, because no axis is now perfectly aligned with the two objects for the entire duration of the detumbling.

As it can be seen, all components of the angular momentum are decreased uniformly, but there is still no effect in the angular velocity around the symmetry axis. The reason can be found in the small magnitude of the torques around this axis, around 5×10^{-7} N · m compared to the 1×10^{-4} N · m around the other ones. Because the torque is so low, the error in torque estimation $\boldsymbol{\epsilon}_L$ (i.e., around 10^{-7}, 10^{-6} N · m) prevents the detumbling from happening. In fact, if the same number of spheres is given to both controller and physics model, there is a slight decrease in $\boldsymbol{\omega}_3$, but this, of course, represents an ideal case because the service spacecraft could never have a perfect knowledge of the debris charge distribution.

It should be noted how it has been demonstrated in previous studies [43] that the relative orbit between the two bodies can influence the performances of the detumbling, and there is a way to exploit this to obtain better results. For simplicity, this is not part of this study because it can be considered as an added bonus that does not influence the validity of the cases analyzed.

IV. Robustness to Uncertainties and Disturbances

An important goal of this study was to obtain a numerical quantification of the effect of system parameter uncertainty on the stability and performance of detumbling. Previously, it was shown how this can be obtained for the error in torque estimation $\boldsymbol{\epsilon}_L$, but this can be further expanded by adding different contributions to the errors, like solar radiation pressure, or most important, errors in the estimated inertia matrix and c.m. of the debris.

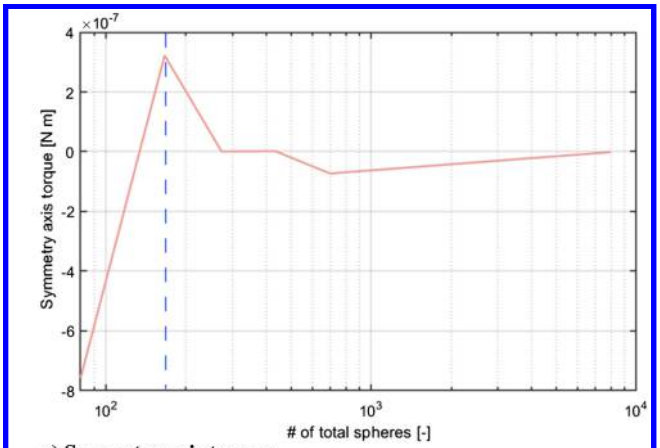

a) Symmetry axis torque

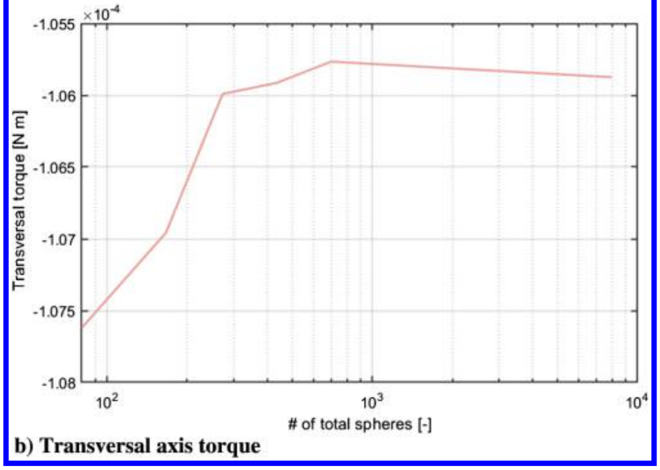

b) Transversal axis torque

Fig. 8 Torque on the debris for different sphere counts.

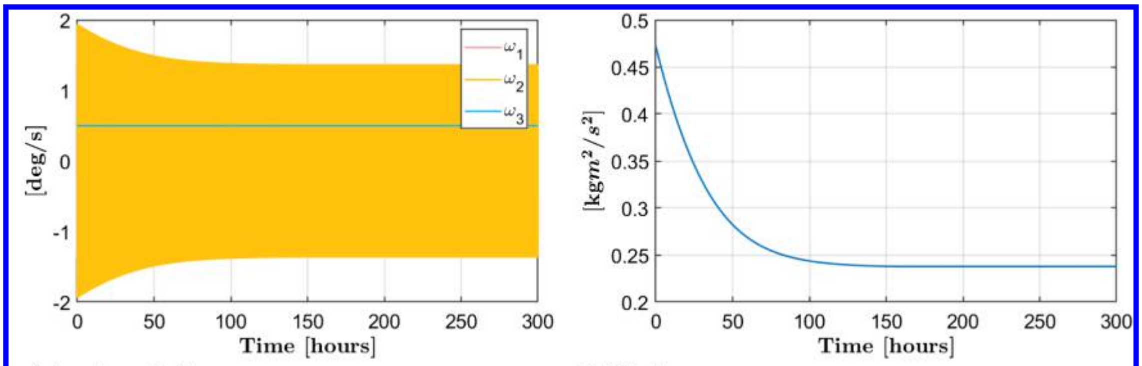

a) Angular velocity

b) Kinetic energy

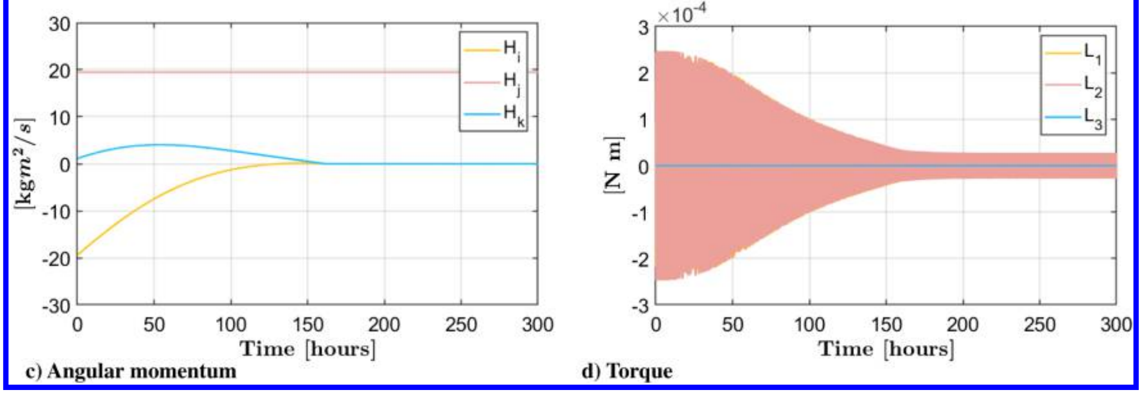

c) Angular momentum

d) Torque

Fig. 9 Spherical service and cylindrical debris for VMSM controller and SMSM controller with 56 sphere debris and 60 sphere service.

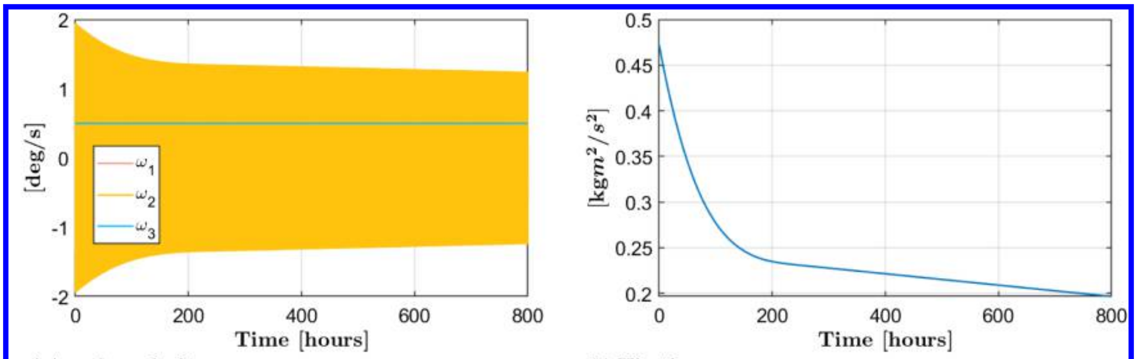

a) Angular velocity

b) Kinetic energy

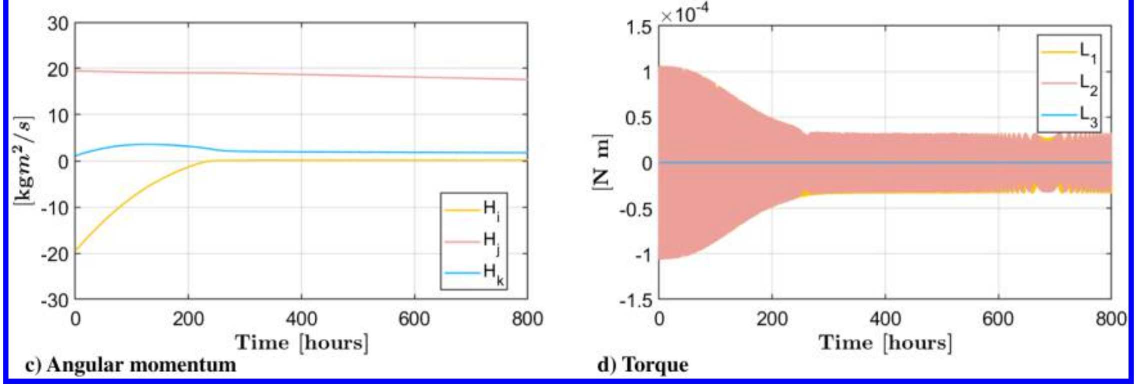

c) Angular momentum

d) Torque

Fig. 10 Satellite service and cylindrical debris, respectively, 68–84 spheres SMSM controller, 160–112 spheres physics.

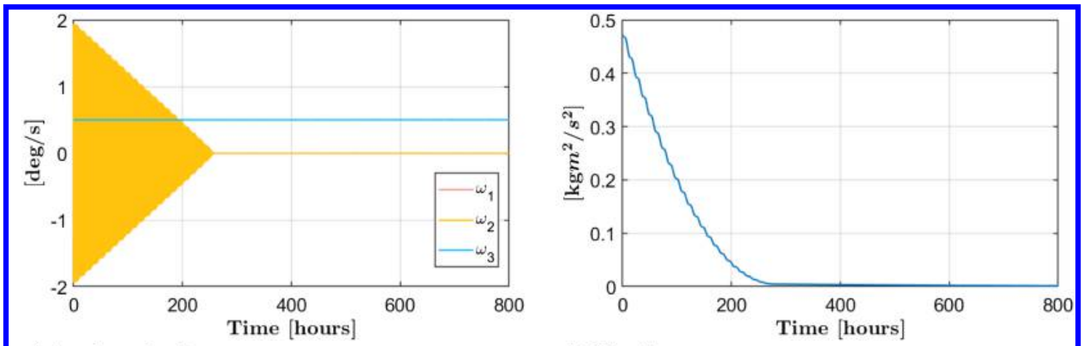

a) Angular velocity

b) Kinetic energy

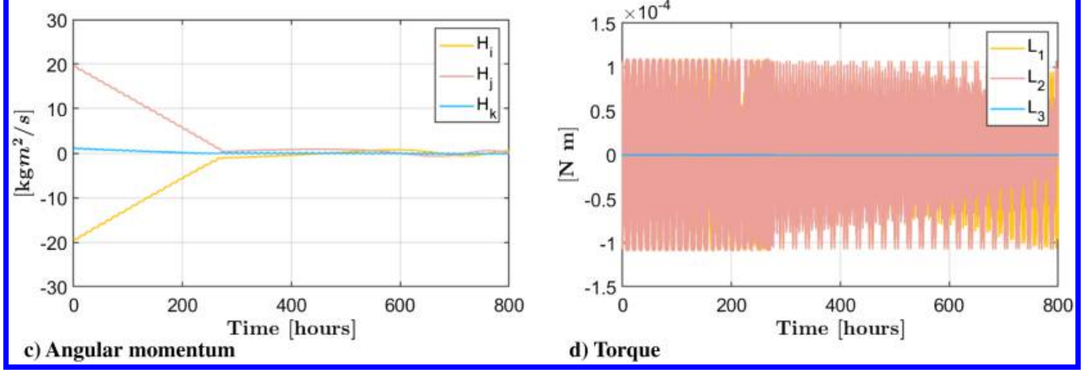

c) Angular momentum

d) Torque

Fig. 11 Same spheres as in Fig. 10, but the debris completes a rotation around the service every 24 h.

This is the first time that this kind of analysis is conducted for an electrostatic detumbling system. The effects of c.m. deviation have been analyzed before, but only in terms of controllability of the system [44], and so it was not stated what would happen if the c.m. of the debris is different from the one the controller expects.

This can easily be modeled in the system by adding a contribution to the torque in Eq. (7):

$$\boldsymbol{L} = \sum_{j=1}^{M} (\boldsymbol{r}_{j|b} - \boldsymbol{\delta}) \times \boldsymbol{F}_j = \sum_{j=1}^{M} \boldsymbol{r}_{j|b} \times \boldsymbol{F}_j + \sum_{j=1}^{M} (-\boldsymbol{\delta}) \times \boldsymbol{F}_j = \boldsymbol{L}_I + \boldsymbol{L}_d \tag{10}$$

So, the real torque is now composed of two contributions: the first $\boldsymbol{L}_I$ given by computing the torque from the ideal position of the c.m. and the second one $\boldsymbol{L}_d$ from its deviation. The latter is only present in the physics model, while in the controller, there is only the expected total torque $\boldsymbol{L}^*$.

Also, the expected torque $\boldsymbol{L}^*$ and the error in torque estimation $\boldsymbol{\epsilon}_L$ can be changed to $\boldsymbol{L}_I^*$ and $\boldsymbol{\epsilon}_I$ for clarity because they refer to the estimate of the ideal torque $\boldsymbol{L}_I$ with respect to the ideal c.m.

This way, it is easy to see that the kinetic energy derivative [Eq. (9)] now has the same contribution as before regarding the ideal torque and another one given by the deviation in the c.m.:

$$\dot{T} = \boldsymbol{\omega}^T \boldsymbol{L}_I^* + \boldsymbol{\omega}^T (\boldsymbol{\epsilon}_I + \boldsymbol{L}_d) \tag{11}$$

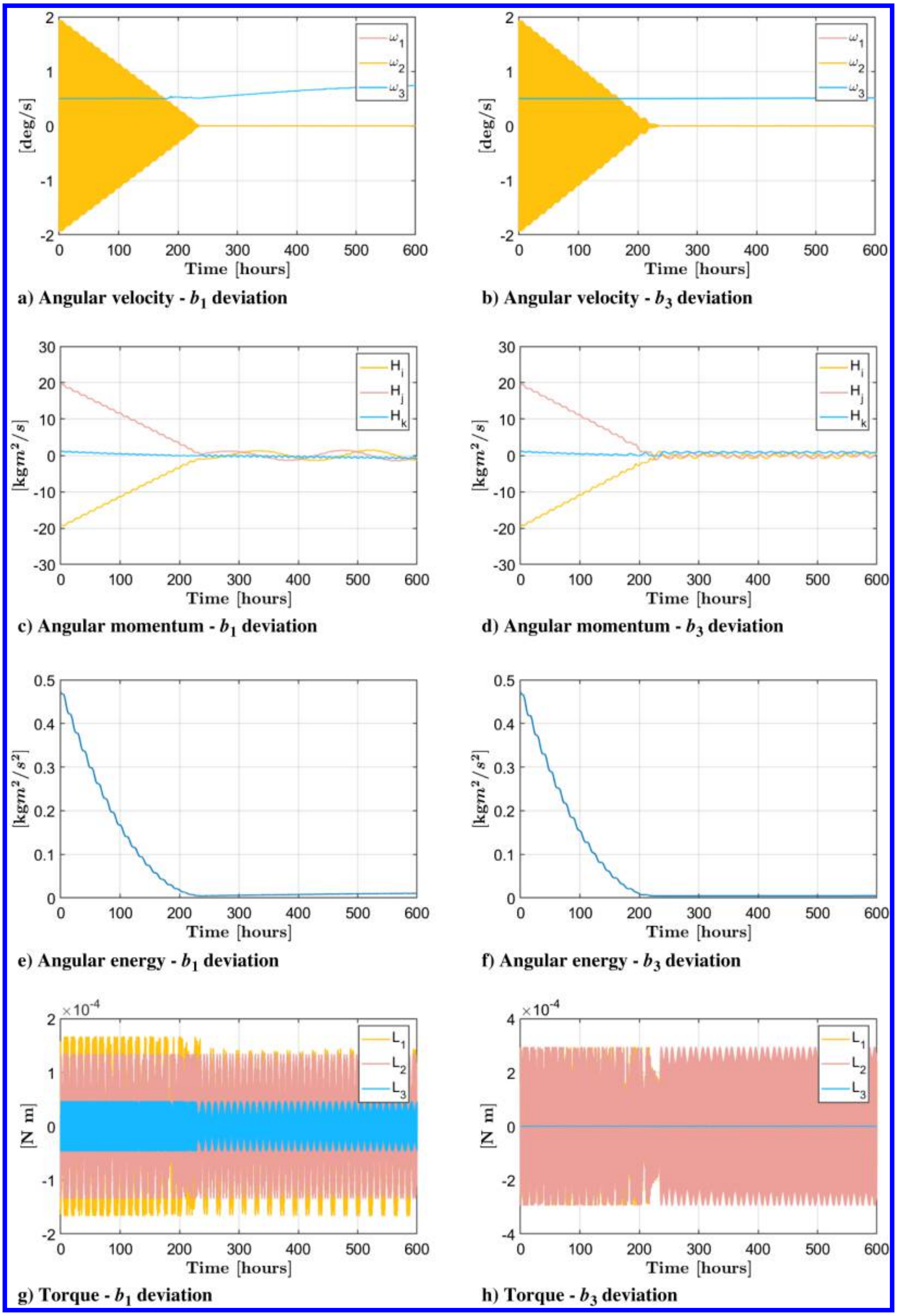

a) Angular velocity - b_1 deviation

b) Angular velocity - b_3 deviation

c) Angular momentum - b_1 deviation

d) Angular momentum - b_3 deviation

e) Angular energy - b_1 deviation

f) Angular energy - b_3 deviation

g) Torque - b_1 deviation

h) Torque - b_3 deviation

Fig. 12 Stability analysis for c.m. deviation along b_1 in the first column and b_3 in the second one.

To better understand how different deviations affect the system, simulations with $\boldsymbol{\delta}$ components only along one axis at the time have been performed. Again, the specifics of the parameters used can be found in the Appendix.

As it can be seen, the system is not significantly affected by the deviations of the c.m. position, but there is still a small increase in $\boldsymbol{\omega}_3$ that if not appropriately handled could lead to unstable behavior.

In fact, if the simulation is repeated with a lower sphere count for the controller debris model, the results in Fig. 12 are obtained.

If the c.m. is moved from the symmetry axis, the system reaches instability very quickly, even 2 cm is enough to cause unstable behavior of $\boldsymbol{\omega}_3$. This demonstrates how sensitive the rotation around this axis can be to the model used, as highlighted in Sec. III.C, and so great care must be taken when selecting the sphere count to use.

As expected, the system is much more stable to deviations of the c.m. along the symmetry axis that do not lead to instability for reasonable deviations; only the total detumbling time can be affected by big-enough δ_3.

Moreover, it is interesting to see how the increase in angular velocity happens only after the other two components have been brought to almost zero. This is a result of the structure of the controller that tends to prioritize potentials that give torques around the first two axes, as these also grant higher torques on the debris, thus decreasing the kinetic energy the most. Once both these components are brought to zero, the controller tries to use the small torques around $\boldsymbol{b}_3$, given only by the induced effects and asymmetries of the charge distribution model, to further decrease the kinetic energy, but because the resulting torque is different because of the deviation component, the angular velocity can end up increasing uncontrollably, as the system has no way of dealing with this effect.

To avoid any possible increase of the angular velocity around this weakly controllable axis, the following two main solutions can be adopted:

1) Because the unstable behavior manifests itself only after $\boldsymbol{\omega}_1$ and $\boldsymbol{\omega}_2$ are brought to zero, the controller could be set up to turn itself off after the components of kinetic energy ($T_i = I_i \omega_i^2$) that depend on those two are decreased below a certain portion of the third one (T_1 and $T_2 < kT_3$). This way, the system is able to detumble most of the debris kinetic energy without incurring in any unstable behavior. This strategy is simple and effective, but has some significant issues. First, it completely removes any possible control authority on the symmetry axis, which could be a problem if the angular velocity around it is too big to be acceptable, and also it relies on the ability of the system to recognize which axis would yield the lowest torque, and thus be more susceptible to unstable behavior. This is not a simple task to accomplish and could require more work than reasonably possible, to set up correctly.

2) A better alternative would be to estimate the deviation torque $\boldsymbol{L}_d$ and other disturbances in the system, and use this to predict instabilities and avoid them. Easier said than done, there is a method developed in the last decade called ADRC that has already proved very useful in many applications [32–35]. This has been found to be very effective in the cases analyzed, and a more in-depth explanation of its structure is given in the next section.

A. Active Disturbance Rejection Control

This control strategy is effective in cases where the disturbances in the system are uncertain, which is the case of debris detumbling. These are often objects in which very little information is available, apart from what can be observed from the outside. More insight could be obtained if the objective of the detumble is a known satellite or spacecraft so that the blueprints and internal structure can be analyzed, but even then there could be some unexpected amount of fuel left in some tanks or some parts of the structure could be missing. In general, it is impossible to know exactly all proprieties of the debris and in particular the position of the c.m. and the inertia. The ADRC works by using an extended state observer to reconstruct the differences between the modeled system and the real one, by lumping all the differences together as a single disturbance torque. Moreover, by splitting the inertia in the expected and uncertain parts, it can be written:

$$
\begin{aligned}
[J]\dot{\boldsymbol{\omega}} &= ([J]^* + [\Delta J])\dot{\boldsymbol{\omega}} = ([J]^* + [\Delta J])\boldsymbol{\omega} \times \boldsymbol{\omega} + \boldsymbol{L} \\
[J]^*\dot{\boldsymbol{\omega}} &= [J]^*\boldsymbol{\omega} \times \boldsymbol{\omega} + \boldsymbol{L}_I^* + \underbrace{[\Delta J]\boldsymbol{\omega} \times \boldsymbol{\omega} - [\Delta J]\dot{\boldsymbol{\omega}} + \boldsymbol{L}_D + \boldsymbol{\epsilon}_I} \\
[J]^*\dot{\boldsymbol{\omega}} &= [J]^*\boldsymbol{\omega} \times \boldsymbol{\omega} + \boldsymbol{L}_I^* + \boldsymbol{d}
\end{aligned} \tag{12}
$$

This way, the real system can be described using the expected values plus an unknown $\boldsymbol{d}$ that includes all unexpected contributions to the dynamics of the system. The extended state observed, taken from [32,34] is given by

$$
\begin{cases}
[J]^*\dot{\boldsymbol{\omega}}^* & = [J]^*\boldsymbol{\omega}^* \times \boldsymbol{\omega}^* + \boldsymbol{L}_I^* + \boldsymbol{d}^* + \beta_1(\boldsymbol{\omega} - \boldsymbol{\omega}^*) \\
\dot{\boldsymbol{d}}^* & = \beta_2(\boldsymbol{\omega} - \boldsymbol{\omega}^*)
\end{cases} \tag{13}
$$

So, by comparing the real angular velocity $\boldsymbol{\omega}$ of the debris (given by the sensors on the service spacecraft) to the expected one $\boldsymbol{\omega}^*$, an estimate $\dot{\boldsymbol{d}}^*$ of the disturbance derivative $\dot{\boldsymbol{d}}$ is obtained, and once integrated, fed into the controller to correct the computed value of the Lyapunov function $\dot{T}^*$ that is now written as

$$
\dot{T}^* = \boldsymbol{\omega}^T(\boldsymbol{L}_I^* + \boldsymbol{d}^*) \tag{14}
$$

Again, the controller checks the value of $\dot{T}^*$ for positive and negative service electric potentials, and picks the one that gives a negative $\dot{T}^*$. There are some drawbacks in this though, because as the value of $\boldsymbol{d}^*$ is received as an input from the controller, it acts as a constant, when in reality it also depends from the chosen potential.

The system is then forced to assume the value of $\boldsymbol{d}^*$ originated from the last time step of integration, generating some inaccuracies that could prove significant if the state of the object couple changes very quickly. To avoid this, the ADRC would need to be able to estimate the separate components of $\boldsymbol{d}^*$ [given in Eq. (12)], so that the component relative to the deviation torque $\boldsymbol{L}_I^*$ could be changed. The authors have not found a way to achieve this yet.

In the cases examined, the evolution of the system is so slow that this does not seem to hinder the efficiency of the control; regardless, it is still something to take into consideration during the analysis.

This updated Lyapunov derivative, when added and subtracted to the real kinetic energy derivative, gives

$$
\dot{T} = \boldsymbol{\omega}^T\boldsymbol{L} = \boldsymbol{\omega}^T(\boldsymbol{L} + \boldsymbol{L}_I^* + \boldsymbol{d}^* - \boldsymbol{L}_I^* - \boldsymbol{d}^*) \tag{15}
$$

Expanding the contributions of $\boldsymbol{L}$ and the lumped sum $\boldsymbol{d}^*$ into its components (The term $\boldsymbol{\epsilon}_I^*$ is not included because it is several order of magnitudes smaller than other components of $\boldsymbol{d}^*$, and so it is not picked up by the state observer, unless the precision given is very high.), and deleting the perpendicular term, it becomes

$$
\begin{aligned}
\dot{T} &= \boldsymbol{\omega}^T(\boldsymbol{L}_I + \boldsymbol{L}_d + \boldsymbol{L}_I^* + \boldsymbol{d}^* - \boldsymbol{L}_I^* - \boldsymbol{d}^*) \\
&= \boldsymbol{\omega}^T(\boldsymbol{L}_I^* + \boldsymbol{d}^*) + \boldsymbol{\omega}^T(\boldsymbol{L}_I - \boldsymbol{L}_I^* + \boldsymbol{L}_d - \boldsymbol{L}_d^* + [\Delta J]^*\dot{\boldsymbol{\omega}}) \\
&= \boldsymbol{\omega}^T(\boldsymbol{L}_I^* + \boldsymbol{d}^*) + \boldsymbol{\omega}^T(\boldsymbol{\epsilon}_I + \boldsymbol{\epsilon}_d + [\Delta J]^*\dot{\boldsymbol{\omega}})
\end{aligned} \tag{16}
$$

Similarly to before, there is a first term that is always negative because it is selected as such by the controller (has a value of around -5×10^{-5} $(\mathrm{kg} \cdot \mathrm{m}^2)/\mathrm{s}^2$ for the case shown as follows), and a second one given by the estimation errors of ideal deviation torque (10^{-7} $(\mathrm{kg} \cdot \mathrm{m}^2)/\mathrm{s}^2$) and the estimated inertia uncertainty (2×10^{-5} $(\mathrm{kg} \cdot \mathrm{m}^2)/\mathrm{s}^2$). The error in torque estimation depends greatly on how quickly the torque imposed changes, and so it will be higher when the system switches potential very quickly. In this example, the last contribution is the most significant and the one that is most likely to degrade the performances of the system; this is a product of the way the ADRC estimates the unknown $\boldsymbol{d}$. Because it is a lumped sum, there is no way to select the different contributions, and so the term given by the change in inertia is present and it cannot be decreased without obtaining a better knowledge of the debris mass proprieties.

The plots in Fig. 15 show some of the cases analyzed and give a plain picture of how this improved control law is able to handle increasing deviations of the c.m. and inertia uncertainties. Again, the specifics are given in the Appendix.

The ADRC is able to effectively detect and use the unexpected c.m. deviation, and the higher the deviation is, the easier it is for the system to control and detumble the debris. As it can be seen, all the cases on the bottom row where the deviation is double in magnitude (but has the same direction) are able to reduce the rotations along the symmetry axis faster. On the other hand, the bigger the $[\Delta J]$ is, the more time the system needs to completely detumble the debris.

If the same deviations and inertia uncertainty are given but with the 33 lower sphere count of Fig. 13, the results in Fig. 16 are obtained.

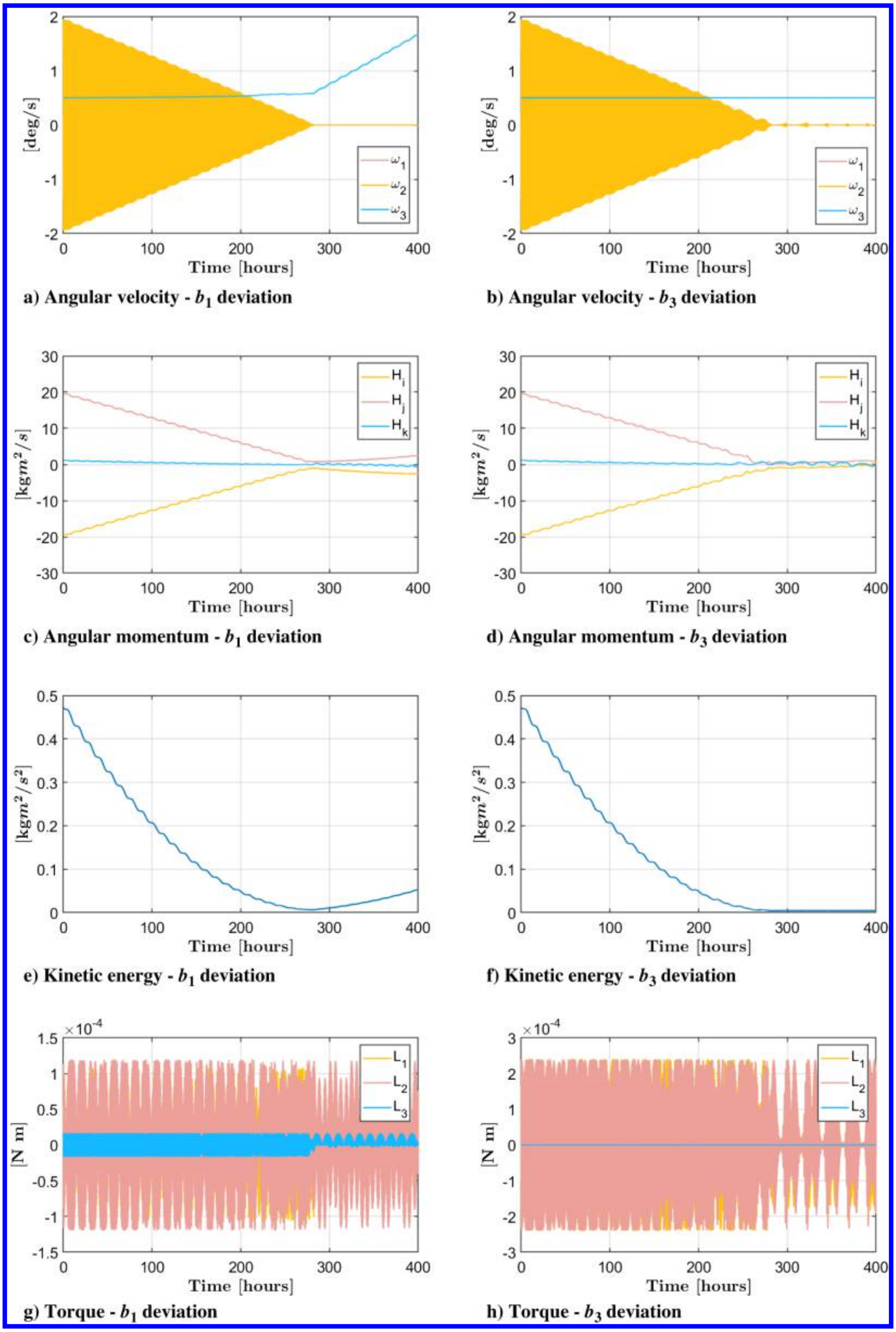

a) Angular velocity - b_1 deviation

b) Angular velocity - b_3 deviation

c) Angular momentum - b_1 deviation

d) Angular momentum - b_3 deviation

e) Kinetic energy - b_1 deviation

f) Kinetic energy - b_3 deviation

g) Torque - b_1 deviation

h) Torque - b_3 deviation

Fig. 13 System with c.m. deviation and controller spheres of debris reduced to 56.

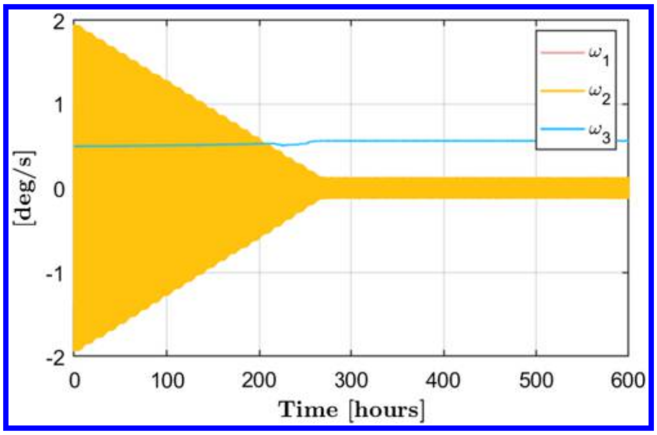

Fig. 14 Angular velocity with shutoff control in unstable case.

The improved control is still able to grant total detumbling in the cases with lower inertia uncertainty, but higher $[\Delta J]$ can considerably slow down the detumbling and also lead to an increase in $\boldsymbol{\omega}_3$.

So, although the ADRC has proved to be a powerful tool that considerably improves the robustness and performance of the system, it is still necessary to select precise-enough sphere models to ensure a correct behavior of the system, especially when there is no precise knowledge of the debris inertia.

It is then advisable for the service spacecraft to spend some time before the detumbling to analyze the free rotations of the debris and try to reconstruct an inertia matrix with the help of LIDAR and image-processing algorithms, like [39–41].

Also, the gains β_1 and β_2 do not need to be changed for each different use, because they only depend on the speed at which the system needs to work and that is based on the angular velocity of the debris itself.

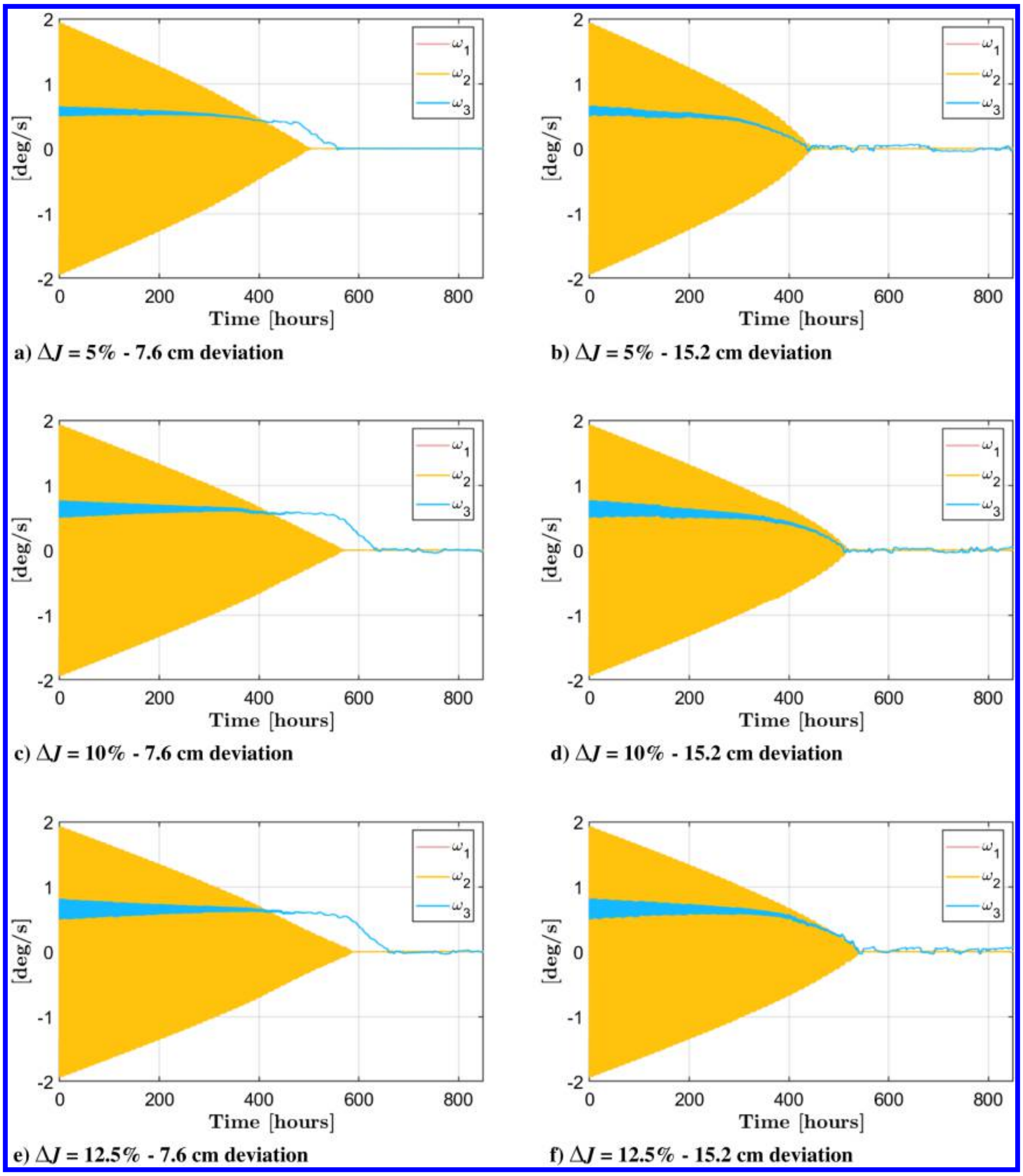

a) ΔJ = 5% - 7.6 cm deviation

b) ΔJ = 5% - 15.2 cm deviation

c) ΔJ = 10% - 7.6 cm deviation

d) ΔJ = 10% - 15.2 cm deviation

e) ΔJ = 12.5% - 7.6 cm deviation

f) ΔJ = 12.5% - 15.2 cm deviation

Fig. 15 Results with 68–84 spheres controller; 160–112 spheres physics with ADRC improved control.

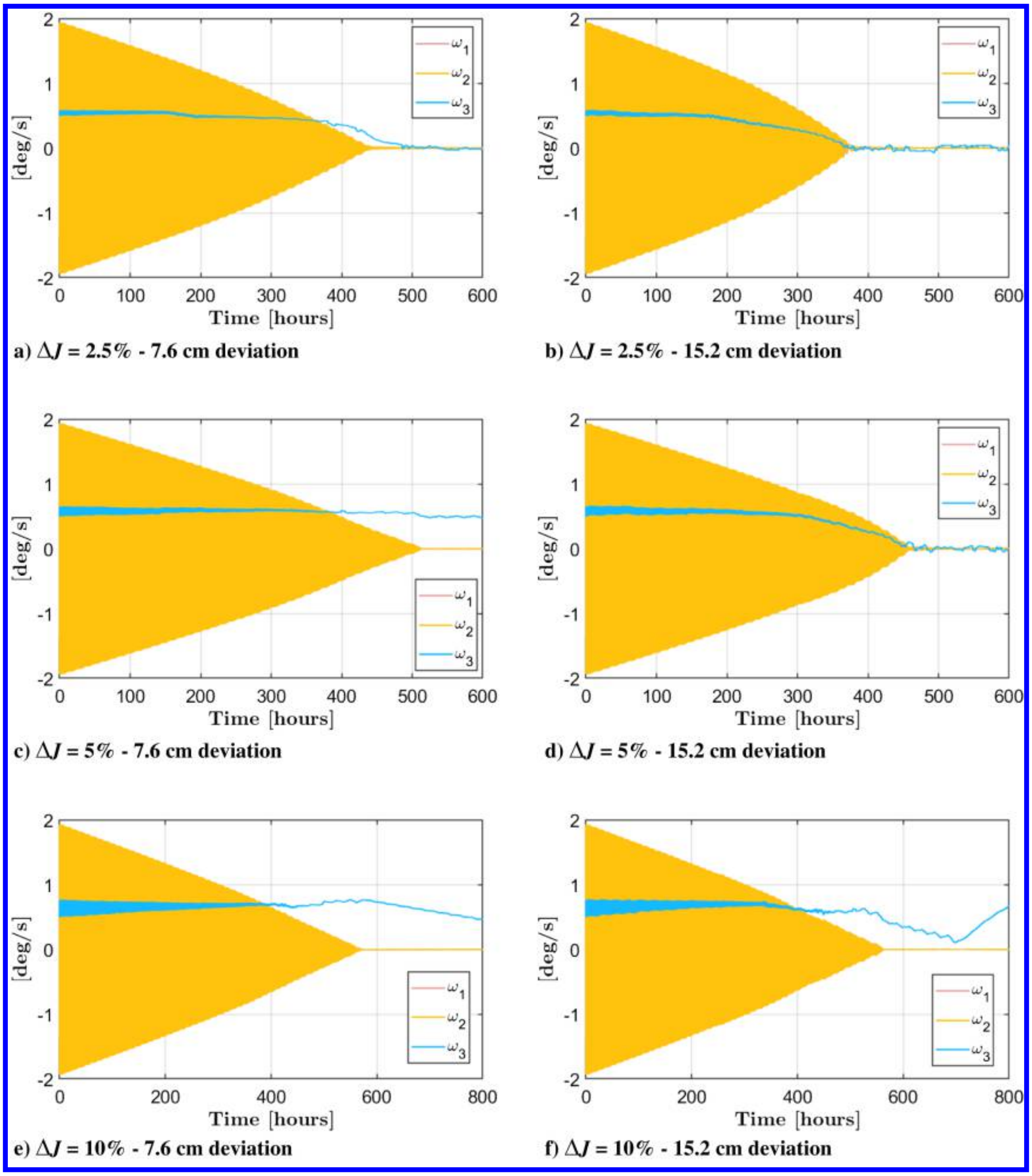

a) $\Delta J = 2.5\%$ - 7.6 cm deviation

b) $\Delta J = 2.5\%$ - 15.2 cm deviation

c) $\Delta J = 5\%$ - 7.6 cm deviation

d) $\Delta J = 5\%$ - 15.2 cm deviation

e) $\Delta J = 10\%$ - 7.6 cm deviation

f) $\Delta J = 10\%$ - 15.2 cm deviation

Fig. 16 Results with 68–56 spheres controller; 160–112 spheres physics with ADRC improved control.

V. Conclusions

The SMSM has proved an effective model to describe the charge distribution in a generic body, without any constraints on its shape. The torques and forces acting on the objects can be correctly computed at faster than real-time speed if the number of spheres considered is appropriate. Using these models, the Lyapunov optimal control law is able to correctly decrease the kinetic energy of the debris, even when accounting for imprecision in the model used.

When the debris is axisymmetric, the controllability is greatly reduced along the symmetry axis, because the system is not able to generate large-enough torques. If the sphere model used is not precise enough, the axisymmetric system is unstable to small deviations of the c.m. along transversal axes, and so great care must be taken in selecting models with an appropriate sphere count. The introduction of an ADRC improves both the robustness and performance considerably, granting a complete detumble for all analyzed cases with a precise-enough model. In addition, for a lower sphere count model, the unstable behavior is avoided if the uncertainty in the inertia components is less than 10%.

In future work, more cases and different geometries should be analyzed to gain a better understanding of how the geometry of the service spacecraft affects the control performance. Moreover, the impact of the attitude of the service spacecraft on the control performance could be modeled, too. It may be possible to optimize the detumbling control further by changing also the attitude of the service spacecraft.

Another possible improvement could be to develop an ADRC that does not assume the expected disturbance as a constant, given by the previous time step, but it is able to select it based on the chosen potential of the bodies. This would improve the effectiveness of the system in cases where the imposed potential changes very quickly.

Appendix: Numerical Simulation Parameters

In this section, the data used to obtain the results and plots present in the paper are given; in particular, the parameters and dimensions of the objects that have been examined, the initial conditions that have been considered, and the deviations and uncertainties that have been randomly selected for testing the ADRC. In all cases, unless stated otherwise, the initial angular velocities and initial quaternion vector are, respectively, $\boldsymbol{\omega}_{B0} = [-1.374; 1.374; 0.5]$ [deg/s] and $\boldsymbol{q}_0 = [0; 0; 0; 1]$.

Table A1 Simulation data for cases with no uncertainties

Parameter	Value	Description
Data for sphere and cylinder debris case in Fig. 9		
R_s	2 m	Spherical spacecraft radius
R_d	1 m	Cylinder radius
h	3 m	Cylinder height
I_1	$125\ \text{kg}\cdot\text{m}^2$	Debris axial inertia
I_2, I_3	$812.5\ \text{kg}\cdot\text{m}^2$	Debris transverse inertia
$V_{\max}$	± 20 kV	Maximum potential imposed
$R_1 - R_3$	0.5909 m	External sphere radius
R_2	0.6512 m	Middle sphere radius
l	1.1569 m	External sphere offset from center of cylinder
R_{deb}	1.7334–1.4313	Capacitance match parameter for debris spheres (56–112)
R_{serv}	1.9–1.9	Capacitance match parameter for service spheres (60–100)
Data for cubic spacecraft and cylinder debris case in Fig. 10		
L_c	$1\times1\times1$ m	Cubic spacecraft size
L_p	2×1 m	Solar panel size
R_d	1 m	Cylinder radius
h	3 m	Cylinder height
I_1	$125\ \text{kg}\cdot\text{m}^2$	Debris axial inertia
I_2, I_3	$812.5\ \text{kg}\cdot\text{m}^2$	Debris transverse inertia
$V_{\max}$	± 20 kV	Maximum potential imposed
R_{deb}	1.628–1.4313	Capacitance match parameter for debris spheres (84–112)
R_{serv}	1.3180–1.3420	Capacitance match parameter for service spheres (68–160)

Table A2 Simulation data for cases with uncertainties

Parameter	Value	Description
Data for unstable cases in Figs. 11–13		
L_c	$1\times1\times1$ m	Cubic spacecraft size
L_p	2×1 m	Solar panel size
R_d	1 m	Cylinder radius
h	3 m	Cylinder height
I_1	$125\ \text{kg}\cdot\text{m}^2$	Debris axial inertia
I_2, I_3	$812.5\ \text{kg}\cdot\text{m}^2$	Debris transverse inertia
$V_{\max}$	± 20 kV	Maximum potential imposed
$\lvert\delta_1\rvert\lvert\delta_2\rvert$	2 cm	C.M. deviation along transversal axis
$\lvert\delta_3\rvert$	20 cm	C.M. deviation along symmetry axes
Data for control shutoff and no inertia uncertainty case in Fig. 14		
L_c	$1\times1\times1$ m	Cubic spacecraft size
L_p	2×1 m	Solar panel size
R_d	1 m	Cylinder radius
h	3 m	Cylinder height
I_1	$125\ \text{kg}\cdot\text{m}^2$	Debris axial inertia
I_2, I_3	$812.5\ \text{kg}\cdot\text{m}^2$	Debris transverse inertia
$V_{\max}$	± 20 kV	Maximum potential imposed
$\lvert\boldsymbol{\delta}_1\rvert, \lvert\boldsymbol{\delta}_2\rvert$	2 cm	C.M. deviation along transversal axis
$\lvert\boldsymbol{\delta}_3\rvert$	20 cm	C.M. deviation along symmetry axes
k	3	Shutoff condition
Data for ADRC case in Figs. 15 *and* 16		
L_c	$1\times1\times1$ m	Cubic spacecraft size
L_p	2×1 m	Solar panel size
R_d	1 m	Cylinder radius
h	3 m	Cylinder height
I_1	$125\ \text{kg}\cdot\text{m}^2$	Debris axial inertia
I_2, I_3	$812.5\ \text{kg}\cdot\text{m}^2$	Debris transverse inertia
$V_{\max}$	± 20 kV	Maximum potential imposed
$\boldsymbol{\delta}$	$[4,\quad -2.5\quad 6]$ and [8] cm	C.M. deviations considered
$[\Delta J_1]$ percentage	5–10–12.5%	Uncertainty on all elements of inertia matrix for Fig. 15
$[\Delta J_2]$ percentage	2.5–5–10%	Uncertainty on all elements of inertia matrix for Fig. 16
β_1, β_2	0.5–50	Full state observer gains

The integration method used is ode113 with relative and absolute tolerances of 10^{-9} and 10^{-8}.

Also, when inertia matrix uncertainties are considered, the unknown real $[J]$ is obtained by adding a certain percentage of the mean inertia value of the ideal one to all elements multiplied by a random number between 0 and 1.

References

[1] Oltrogge, D. L., Alfano, S., Law, C., Cacioni, A., and Kelso, T. S., "A Comprehensive Assessment of Collision Likelihood in Geosynchronous Earth Orbit," *Acta Astronautica*, Vol. 147, June 2018, pp. 316–345.
https://doi.org/10.1016/j.actaastro.2018.03.017

[2] Jehn, R., and Hernandez, C., "International Practices to Protect the Geostationary Ring," *Space Debris*, Vol. 1, Dec. 2001, pp. 221–233.
https://doi.org/10.1016/j.actaastro.2013.08.023

[3] Jehn, R., Agapov, V., and Hernandez, C., "The Situation in the Geostationary Ring," *Advances in Space Research*, Vol. 35, No. 7, 2005, pp. 1318–1327.
https://doi.org/10.1016/j.asr.2005.03.022

[4] Anderson, V., and Schaub, H., "Local Debris Congestion in the Geosynchronous Environment with Population Augmentation," *Acta Astronautica*, Vol. 94, No. 2, 2014, pp. 619–628.
https://doi.org/10.1016/j.actaastro.2013.08.023

[5] Johnson, N., "Protecting the Geo Environment: Policies and Practices," *Space Policy*, Vol. 15, No. 3, 1999, pp. 127–135.
https://doi.org/10.1016/S0265-9646(99)00022-3

[6] Chrystal, P., McKnight, D., Meredith, P. L., Schmidt, J., Fok, M., Chrystal, C. W., McKnight, D., Meredith, P. L., Jan Schmidt, M. F., and Wetton, C., "Space Debris: On Collision Course for Insurers," Tech. Rept., Swiss Reinsurance, March 2011.

[7] Caubet, A., and Biggs, J., "Design of an Attitude Stabilization Electromagnetic Module for Detumbling Uncooperative Targets," *IEEE Aerospace Conference*, IEEE, New York, 2014.
https://doi.org/10.1109/AERO.2014.6836325

[8] Couzin, P., Teti, F., and Rembala, R., "Active Removal of Large Debris: Rendezvous and Robotic Capture Issues," *2nd European Workshop on Active Debris Removal*, Paris, France, 2012, Paper #7.5.

[9] Couzin, P., Teti, F., and Rembala, R., "Active Removal of Large Debris: System Approach of Deorbiting Concepts and Technological Issues," *6th European Conference on Space Debris*, ESA SP-723, Darmstadt, Germany, April 2013, Paper 25.

[10] Kaplan, M. H., "Dynamics and Control of Detumbling a Disabled Spacecraft During Rescue Operations," NASA CR-135788, AAR-73-10, 1973.

[11] Gangapersaud, R. A., Liu, G., and Ruiter, A. H., "Detumbling a Non-Cooperative Target with Unknown Inertial Parameters Using a Space Robot Under Control Input Magnitude Constraint," *Advances in Space Research*, Vol. 63, No. 12, 2019, pp. 3900–3915.

[12] Bennett, T., and Schaub, H., "Touchless Electrostatic Three-Dimensional Detumbling of Large Axi-Symmetric Debris," *Journal of the Astronautical Sciences*, Vol. 62, Nov. 2015, pp. 233–254.
https://doi.org/10.1007/s40295-015-0075-8

[13] Karavaev, Y. S., Kopyatkevich, R. M., Mishina, M. N., Mishin, G. S., Papushev, P. G., and Shaburov, P. N., "The Dynamic Properties of Rotation and Optical Characteristics of Space Debris at Geostationary Orbit," *Advances in the Astronautical Sciences*, Vol. 4, No. 119, 2005, pp. 1457–1466.

[14] Karavaev, Y. S., Mishina, M. N., and Papushev, P. G., "Investigations of the Evolution of Optical Characteristics and Dynamics of Proper Rotation of Uncontrolled Geostationary Artificial Satellites," *Advances in Space Research*, Vol. 43, No. 9, 2009, pp. 1416–1422.

[15] Aslanov, V. S., and Ledkov, A. S., "Attitude Motion of Cylindrical Space Debris During Its Removal by Ion Beam," *Mathematical Problems in Engineering*, Vol. 2017, Nov. 2017, Paper 1986374.
https://doi.org/10.1155/2017/1986374

[16] Bombardelli, C., and Peláez, J., "Ion Beam Shepherd for Contactless Space Debris Removal," *Journal of Guidance, Control, and Dynamics*, Vol. 34, No. 3, 2010, pp. 916–920.
https://doi.org/10.2514/1.5183

[17] Bennett, T., Stevenson, D., Hogan, E., and Schaub, H., "Prospects and Challenges of Touchless Electrostatic Detumbling of Small Bodies," *Advances in Space Research*, Vol. 56, No. 3, 2015, pp. 557–568.
https://doi.org/10.1016/j.asr.2015.03.037

[18] Anderson, V., and Schaub, H., "Conjunction Challenges of Low-Thrust Geosynchronous Debris Removal Maneuvers," *Acta Astronautica*, Vol. 123, June–July 2016, pp. 154–164.
https://doi.org/10.1016/j.actaastro.2016.03.014

[19] Schaub, H., and Moorer, D. F., Jr., "Geosynchronous Large Debris Reorbiter: Challenges and Prospects," *Journal of the Astronautical Sciences*, Vol. 59, Nos. 1–2, 2012, pp. 165–180.

[20] Schaub, H., and Sternovsky, Z., "Active Space Debris Charging for Contactless Electrostatic Disposal Maneuvers," *Advances in Space Research*, Vol. 53, No. 1, 2014, pp. 110–118.

[21] Bennett, T., and Schaub, H., "Contactless Electrostatic Detumbling of Axi-Symmetric Geo Objects with Nominal Pushing or Pulling," *Advances in Space Research*, Vol. 62, No. 11, 2018, pp. 2977–2987.
https://doi.org/10.1016/j.asr.2018.07.021

[22] Aslanov, V., and Schaub, H., "Detumbling Attitude Control Analysis Considering an Electrostatic Pusher Configuration," *Journal of Guidance, Control, and Dynamics*, Vol. 42, No. 4, 2019, pp. 900–909.
https://doi.org/10.2514/1.G003966

[23] Tribble, A., *The Space Environment, Implications for Spacecraft Design*, rev. and expanded ed., Princeton Univ. Press, Princeton, NJ, 2003, Chap. 3.

[24] Denton, M. H., Thomsen, M. F., Korth, H., Lynch, S., Zhang, J., and Liemohn, M. W., "Bulk Plasma Properties at Geosynchronous Orbit," *Journal of Geophysical Research*, Vol. 110, No. A7, 2005, p. 17.

[25] Seubert, C. R., Stiles, L. A., and Schaub, H., "Effective Coulomb Force Modeling for Spacecraft in Earth Orbit Plasmas," *Advances in Space Research*, Vol. 54, No. 2, 2014, pp. 209–220.
https://doi.org/10.2514/1.51832

[26] Stevenson, D., and Schaub, H., "Multi-Sphere Method for Modeling Spacecraft Electrostatic Forces and Torques," *Advances in Space Research*, Vol. 51, No. 1, 2013, pp. 10–20.
https://doi.org/10.1016/j.asr.2012.08.014

[27] Maxwell, J., Wilson, K. T. H., Ghanei, M., and Schaub, H., "Multi-Sphere Method for Flexible Conducting Space Objects: Modeling and Experiments," *AAS/AIAA Astrodynamics Specialist Conference*, AAS Paper 18-400, 2018.

[28] Ingram, G., Hughes, J., Bennett, T., Reilly, C., and Schaub, H., "Volume Multi-Sphere-Model Development Using Electric Field Matching," *Journal of the Astronautical Sciences*, Vol. 65, Nov. 2018, pp. 377–399.
https://doi.org/10.1007/s40295-018-0136-x

[29] Chow, P., Hughes, J., Bennett, T., and Schaub, H., "Automated Sphere Geometry Optimization for the Volume Multi Sphere Method," *26th AAS/AIAA Spaceflight Mechanics Meeting*, AAS Paper 17-451, 2016.

[30] Stevenson, D., and Schaub, H., "Optimization of Sphere Population for Electrostatic Multi-Sphere Method," *IEEE Transactions on Plasma Science*, Vol. 41, No. 12, 2013, pp. 3526–3535.
https://doi.org/10.1109/TPS.2013.2283716

[31] Hughes, J. A., and Schaub, H., "Heterogeneous Surface Multisphere Models Using Method of Moments Foundations," *Journal of Spacecraft and Rockets*, Vol. 56, No. 4, 2019, pp. 1259–1266.
https://doi.org/10.2514/1.A34434

[32] Bai, Y., Biggs, J., Zazzera, F. B., and Cui, N., "Adaptive Attitude Tracking with Active Uncertainty Rejection," *Journal of Guidance, Control, and Dynamics*, Vol. 41, No. 2, 2018, pp. 546–554.
https://doi.org/10.2514/1.G002391

[33] Han, J., "From PID to Active Disturbance Rejection Control," *IEEE Transactions on Industrial Electronics*, Vol. 56, No. 3, 2009, pp. 900–906.
https://doi.org/10.1109/TIE.2008.2011621

[34] Bai, Y., Biggs, J. D., Wang, X., and Cui, N., "A Singular Adaptive Attitude Control with Active Disturbance Rejection," *European Journal of Control*, Vol. 35, May 2017, pp. 50–56.
https://doi.org/10.1016/j.ejcon.2017.01.00

[35] Huang, Y., and Xue, W., "Active Disturbance Rejection Control: Methodology and Theoretical Analysis," *ISA Transactions*, Vol. 53, No. 4, 2014, pp. 963–976.
https://doi.org/10.1016/j.isatra.2014.03.003

[36] "3D Builder," 2013, https://www.microsoft.com/it-it/p/3d-builder/9wzdncrfj3t6?activetab=pivot:overviewtab.

[37] Cignoni, P., Callieri, M., Corsini, M., Dellepiane, M., Ganovelli, F., and Ranzuglia, G., "MeshLab: An Open-Source Mesh Processing Tool," 2008. http://www.meshlab.net/.

[38] Maxwell, J., and Schaub, H., "Applicability of the Multi-Sphere Method to Flexible One-Dimensional Conducting Structures," *AAS/AIAA Astrodynamics Specialist Conference*, AAS Paper 17-618, 2017.

[39] Pesce, V., Lavagna, M., and Bevilacqua, R., "Stereovision-Based Pose and Inertia Estimation of Unknown and Uncooperative Space Objects," *Advances in Space Research*, Vol. 59, No. 1, 2017, pp. 236–251.
https://doi.org/10.1016/j.asr.2016.10.002

[40] Tweddle, E., Saenz-Otero, A., Leonard, J. J., and Miller, D. W., "Factor Graph Modeling of Rigid-Body Dynamics for Localization, Mapping, and Parameter Estimation of a Spinning Object in Space," *Journal of Field Robotics*, Vol. 32, No. 6, 2018, pp. 805–817. https://doi.org/10.1002/rob.21548

[41] Volpe, R., Palmerini, G. B., and Sabatini, M., "A Passive Camera Based Determination of a Non-Cooperative and Unknown Satellite's Pose and Shape," *Acta Astronautica*, Vol. 151, Oct. 2015, pp. 233–254. https://doi.org/10.1016/j.actaastro.2018.06.061

[42] Schaub, H., *Analytical Mechanics of Space Systems*, 4th ed., AIAA Education Series, 2018, Chap. 2.

[43] Bennett, T., and Schaub, H., "Capitalizing on Relative Motion in Electrostatic Detumbling of Axi-Symmetric GEO Objects," *6th International Conference on Astrodynamics Tools and Techniques (ICATT)*, Darmstadt, Germany, March 2016.

[44] Hughes, J. A., and Schaub, H., "Spacecraft Electrostatic Force and Torque Expansions Yielding Appropriate Fidelity Measures," *Journal of Astronautical Sciences*, Vol. 66, May 2019, pp. 46–67. https://doi.org/10.1007/s40295-019-00154-7

V. J. Lappas
Associate Editor